MDPI

Article

Ionic Mobility and Charge Carriers Recombination Analyzed in Triple Cation Perovskite Solar Cells

Juan Jose Rodriguez-Perez [1], Asya Mhamdi [2], Jeevan Torres [3], Isaac Montes-Valenzuela [3], Jesus Manuel Rivas [3], Diego Esparza [3,*] and David Armando Contreras-Solorio [1,*]

[1] Unidad Académica de Ciencia y Tecnología de la Luz y la Materia, Universidad Autónoma de Zacatecas, Circuito Marie Curie S/N, Quantum, Zacatecas 98160, Mexico; jjrpkemonito@hotmail.com

[2] Équipe Dispositifs Électroniques Organiques et Photovoltaïque Moléculaire, Laboratoire de la, Matière Condensée et des Nanosciences, Faculté des Sciences de Monastir, Université de Monastir, Avenue de l'environnement, Monastir 5019, Tunisia; mhamdiasya@gmail.com

[3] Unidad Académica de Ingeniería Eléctrica, Universidad Autónoma de Zacatecas, Av. Ramón López Velarde 801, Col. Centro, Zacatecas 98060, Mexico; carlosjeevan@hotmail.com (J.T.); isaacmontesv@gmail.com (I.M.-V.); jmrivas@uaz.edu.mx (J.M.R.)

* Correspondence: desparza@uaz.edu.mx (D.E.); dacs10@yahoo.com.mx (D.A.C.-S.)

Abstract: In this work, a study of a characterization technique based on open circuit voltage decay is carried out to obtain the recombination resistance of mobile charge carriers and ionic migration in triple cation perovskite solar cells. The devices were fabricated with the structure $FTO/TiO_2/Cs_{0.05}FA_{1-X}MA_XPb(I_{1-X}Br_X)_3/spiroOMetad/Au$. An equivalent circuit, created in Ngspice, was developed adjusting the capacitance and resistance values to fit the experimental open circuit voltage (V_{oc}) decay curves observed. The aim of this study is to associate the perovskite ionic migration with the V_{oc} characteristic time of charge transport in triple cation perovskite solar cells. Thus, an analysis of the open circuit voltage transient behavior was made by taking measurements of the photovoltage as a function of time. The results indicate that the technique shows charge recombination while the device is illuminated. In addition, an enhancement of the recombination resistance when increasing the FA^+ concentration was observed. Finally, the transient behavior was associated with MA^+, FA^+, Cs^+ and I^- migration, obtaining an ionic mobility in the range between 10^{-10} to 10^{-12} cm^2 $(Vs)^{-1}$.

Keywords: recombination resistance; equivalent circuit; ionic mobility; fitting analysis

1. Introduction

In recent years, organometallic perovskite solar cells (PSCs) have continued their rapid development, due in part to their increase in efficiency [1], high diffusion length [2], solution processable nature [3], excellent optical properties [4], and economic feasibility [5]. However, their operating principles are still under study [6–11]. Understanding the physical processes in perovskite solar cells is necessary to design and develop long term stable devices. Amongst several advantages of PSCs are: charge carrier diffusion length of about 100 nm [12], charge carrier lifetime of around 270 ns [13], and a high defect tolerance (2.5 I/Pb ratio) [13]. Thus, perovskite solar cells are outperforming other solution processed solar cell technologies [14–17]. However, ion migration is a problem in perovskite solar cells, making it difficult to measure efficiency and to define a steady state condition [18]. In addition to producing J-V hysteresis, ion migration appears as one of the causes of degradation of perovskite solar cells [19,20]. Charge accumulation at the contact determines the behavior of perovskite solar cells [21]. The correlation between the film thickness and device performance is due to interfacial charge accumulation which leads to charge carrier recombination affecting V_{oc} [22]. For the case of ionic and electronic charge transfers, it has

been suggested that the perovskite contacts interact as transistors which couple ionic charge redistribution to energetic barriers controlling electron injection and recombination [23].

Several studies on ion migration have been conducted in perovskite solar cells. The presence of mobile ions and their accumulation at the interfaces has a significant effect on the distribution of the electric field, mainly in the perovskite layer [24–28], which directly affects the charge extraction in the device [25–27]. Thus, to improve our understanding of perovskite solar cells, it seems necessary to better understand the coexistence of electronic and ionic conduction in these devices [18,29].

The aim of this study is to associate the characteristic times of open circuit voltage decay (OCVD) with ionic or vacancy migration in the perovskite layer and charge transport in the device. Therefore, an analysis of the V_{oc} was conducted by photovoltage transient measurements. It is necessary to understand the photovoltage rise and decay profile of perovskite solar cells, which is unusual compared to other types of photovoltaic cells such as dye sensitized solar cells [30]. On photovoltaic cells of previous generations, the photovoltage decay does not show a simple exponential relaxation profile, which means a recombination of electrons and holes of the first order [31].

Measurements of photovoltage decay in open circuit showed magnitudes of time related to the electron-ion coupling kinetics in orders of milliseconds (ms) and seconds (s) as reported by Bauman et al. in 2014 [32]. However, this cooperative "vital relationship", as described by Bertoluzzi et al. in 2015, opened the ion–electron kinetics research area [33]. In the range of our measurements, milliseconds for fast decay and seconds for slow decay are attributed to this cooperative kinetic relationship, mostly dominated in milliseconds for electronic kinetics and seconds for ionic kinetics. For our multiple cation devices, we can relate the slow processes to layers of ionic charge near the selective contacts as described by Bisquert et al. in their description of the physics of perovskite solar cells in 2018 [34]. The photovoltage decay profiles have an asymmetric shape where two decays are observed, one fast and one slow as mentioned above. The fast part is due to the loss of polarization of the perovskite film and the slow part to recombination of interfacial charge as attributed by Wang [5]; however, he found that slow and fast voltage loss are not independent and slow depletion results in a change in the photovoltage decay profile [35]. The study of ion migration is important because this materials class affects the behavior of the solar cells with undesirable hysteresis and degradation in the device, affecting the solar cells [36]. In this work, an alternative technique is presented to obtain the ionic migration by open circuit voltage characteristic time of charge transport.

2. Materials and Methods

Materials: Patterned fluorine-doped tin oxide (FTO)-coated glass substrates (MTI, TEC-15), lead iodide (PbI$_2$, 99.99%, TCI, Tokyo, Japan), lead bromide (PbBr$_2$, TCI, 99.99%), formamidinium iodide (FAI, Dyenamo, >99%, Stockholm, Sweden), methylammonium iodide (MAI, Dyenamo, >98%, Stockholm, Sweden), cesium iodide (CsI, Aldrich, 99.9%, Louis, MO, USA), spiro MeOTAD (LT-S922, 99%, Lumtec, Taiwan), N,N-dimethylformamide (DMF, Aldrich, anhydrous 99.8%, Louis, MO, USA), dimethyl sulfoxide (DMSO, Aldrich, 99.9%, Louis, MO, USA), isopropanol (IPA, Aldrich, anhydrous 99.5%, Louis, MO, USA), lithium salt (LiTFSI, Aldrich, 99.95%, Louis, MO, USA), acetone, acetonitrile, ethanol, and acetylacetone (CH$_3$COCH$_2$COCH$_3$, Honeywell, 99.5%, morris, NJ, USA) were used as purchased.

Device Fabrication: FTO-coated glass substrates were sequentially cleaned in detergent, deionized water, acetone and IPA. First, deposition was compact titanium dioxide (TiO$_2$), by spray pyrolysis. Next, a mesoporous TiO$_2$ was deposited by spin coating at 2000 rpm for 10 s and annealed at 450 °C for 2 h. A lithium salt passivation then followed, and LiTFSI in acetonitrile 10 mg/mL was spin coated at 1000 rpm for 10 s and heated similarly to the mesoporous TiO$_2$. A DMF:DMSO (4:1 V:V) solvent was made to dissolve PbI$_2$ and PbBr$_2$ in a 1.5 M concentration, to be further added at 1.24 M onto FAI and MABr, respectively. MABr$_3$ and CsI were used as dopants for the FAPbI$_3$ structure, considering that the term "doping",

from a materials science perspective, is regarded as intentional introduction of a small amount of impurities into the otherwise pure material, to tune its electronic properties [37]. The CsI were dissolved in DMSO 1.5 M nominal concentration. Mixed perovskites were made according to the experiments. The perovskite film obtained was transferred to a hot plate for annealing at 100 °C for 3 min, forming a dark perovskite film. The spiro-MeOTAD was then spin coated at 1800 rpm for 30 s. Finally, an 80 nm gold film was thermally evaporated as metal electrode. The formula $Cs_{0.05}FA_{1-X}MA_XPb(I_{1-X}Br_X)_3$ was used to prepare the samples. The three samples prepared were: $Cs_{0.05}FA_{0.915}MA_{0.085}Pb(I_{0.915}Br_{0.085})_3$, this sample was named as 0.915; $Cs_{0.05}FA_{0.83}MA_{0.17}Pb(I_{0.83}Br_{0.17})_3$, named as 0.83; and $Cs_{0.05}FA_{0.745}MA_{0.255}Pb(I_{0.745}Br_{0.255})_3$, named as 0.745.

Characterization Methods: Current density–voltage characteristics of perovskite solar cells under 1 sun illumination were obtained. The J–V curves were recorded using a Wavelabs Sinus-70 LED class AAA solar simulator in air and the measurements were carried out using a GAMRY Instruments Reference 600 potentiostat. Current density–voltage curves (J–V curves) were measured from open circuit to short-circuit (reverse scan), with a scan rate of 100 mV/s and a step size of 0.1 mV under a 100 mW/cm2 AM1.5 (1 sun) illumination. The light intensity was calibrated with a Silicon reference cell from Fraunhofer ISE. JV scans were obtained with a Keithley 2400 SMU, controlled by a measurement control program written in LabView. The data were obtained with a voltage step of 10 mV with an integration time of 50 ms per point, and settling time of 50 ms after voltage application, corresponding to a scan rate of 100 mV/s. The device's active area is 0.16 cm^2.

3. Characterization Techniques

3.1. Open Circuit Voltage Decay Measurements

Open circuit voltage decay measurements were carried out in dark conditions for 5 s and then the devices were excited with AM1.5 radiation (100 mW/cm^2) for 10 s, which we will call the excitation time (te). Once this time (te) has elapsed, the illumination is suppressed, and the relation to open circuit voltage decay can be observed in the curve. The open circuit transient profile during illumination and suppression of light is illustrated in the diagram in Figure 1. Figure 1a shows the device in equilibrium in the dark: the Fermi level is the same in the n-type material, the perovskite and the p-type material, so an internal electric field is generated within the perovskite. At the interface between the n-type material and perovskite, the electrons in the conduction band will move from the n-type semiconductor to the perovskite to establish a state of equilibrium. It is known that when a neutral atom loses an electron, it becomes a positive ion; therefore, positive ions are created at the junction of the n-type material, and these ions are in the depletion region forming a Schottky barrier (Figure 1a).The ions within the perovskite move in the electric field neutralizing the field; the anions accumulate at the interface between the n-type material and the perovskite, while the cations accumulate at the interface between the p-type material and perovskite (Figure 1b). When illuminating the device, the TiO_2 accepts the electrons while the Spiro-MeOTAD receives the holes, so the electric field inside the perovskite is reversed in such a way that the anions move to the interface of the p-type material and the cations towards the n-type interface, neutralizing the electric field again (Figure 1c). In the quasi-stable condition under open circuit illumination, cations will accumulate at the n-type material interface, while anions will accumulate at the p-type interface (Figure 1d). In this condition, the electrostatic potential plus the incorporated potential generate the photovoltage reached in the solar cell. At the moment that the illumination is suppressed, the ions of the interfaces accumulate until reaching the equilibrium in darkness again (Figure 1e) [30].
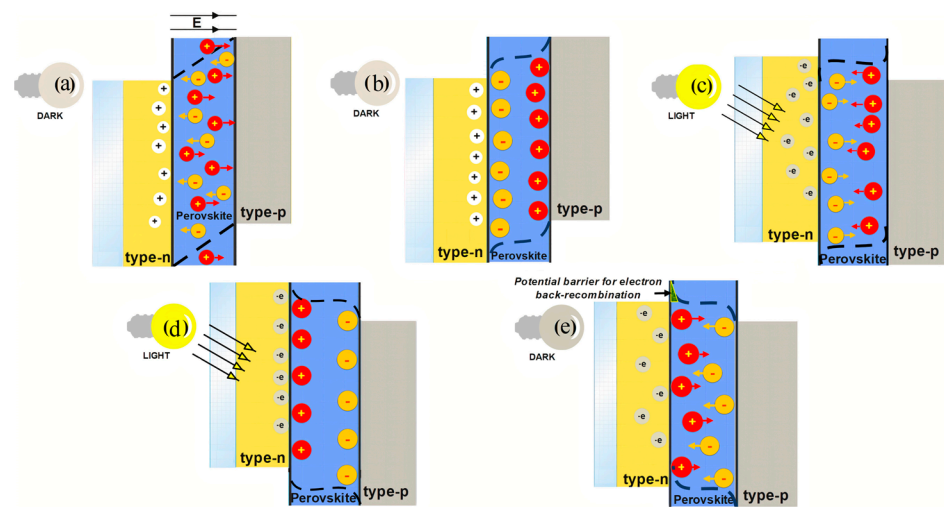
Figure 1. The schematic energy diagram in perovskite absorber layer: (**a**) The device in equilibrium in the dark; the Fermi level is the same in the n-type material, the perovskite and the p-type material, so an internal electric field is generated within the perovskite. (**b**) The ions within the perovskite move in the electric field neutralizing the field, and the anions accumulate at the interface between the n-type material and the perovskite. (**c**) The device is illuminated, the TiO$_2$ accepts the electrons while the Spiro-MeOTAD receives the holes. (**d**) The quasi-stable condition under open circuit illumination. (**e**) The moment that the illumination is suppressed, the ions of the interfaces accumulate until reaching the equilibrium in darkness again.

In the process, the asymmetric peculiarity of the rise and decay of the open circuit voltage is generated due to the accumulation of cations and anions when the illumination is turned on and off, so that in dark equilibrium the anions accumulate near the interface of the n-type material and cations accumulate near the interface of the p-type material; but in almost stable conditions while lighting, the reverse phenomenon occurs, therefore the accumulation of ions at the perovskite interfaces would form a capacitance resulting in the formation of a Schottky barrier and the bending of the energy band, as seen in Figure 1e. Moreover, when the illumination is suppressed, the electrons in the n-type material begin to recombine with the holes in the perovskite, resulting in a fast decay of Voc ($\approx$100 ms). On the other hand, the missing voltage decay depends on the reduction of the Schottky barrier that prevents electrons from recombining in the perovskite. Therefore, the time to exhaust the Schottky barrier depends on the ion concentration in the perovskite structure.

3.2. Equivalent Circuit in PSpice

The rise and decay behavior of the open circuit photovoltage, resulting from the lighting pulse of the solar cell, was reproduced using an equivalent circuit comprising two processes, one for the ionic process (blue) and the other representing the common electronic processes (red) (Figure 2), with a similarity of more than 90%. The circuit is optimized by minimizing the cost function, which is defined as the sum of the absolute differences between the experimental stress values and the simulated stress values, as indicated by equation:

$$J(\theta) = \frac{1}{2m} \sum_{i=1}^{m} \left(h_\theta \left(x^{(i)} \right) - y^{(i)} \right)^2 \tag{1}$$

where $h_\theta \left(x^{(i)} \right)$ corresponds to the experimental stress values and $y^{(i)}$ corresponds to the simulated values.
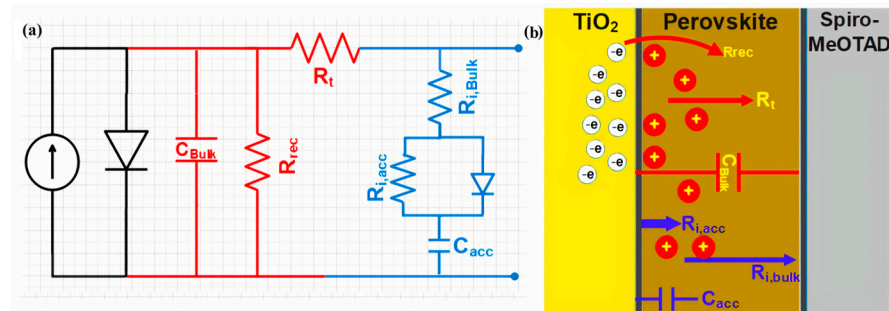
Figure 2. Equivalent circuit with electronic and ionic components (**a**); and schematic of layers of perovskite based solar cells (**b**).

The equivalent circuit is based on the proposal made by F. Ebadi et al. [36]. The electrical circuit diagram of Figure 2 can be explained in the following sections:

1. The first section illustrates the diode and the photogenerated current.
2. The intermediate section contains passive components indicating the bulk capacitance and the free charge carrier resistance to recombine and transport, where R_{rec} refers to the reverse transfer resistance for the recombination of electrons in the solar cells, C_{bulk} represents the global capacitance of perovskite and all types of electric charge storage in the perovskite solar cell, including the geometric ones, and R_t corresponds to the transport resistance of the carriers.
3. The last section includes the bulk and accumulation ionic resistances, the ionic accumulation capacitance and a diode that produces the asymmetric behavior at the time of capacitor discharge, where R_{ibulk} represents the resistance to ion transport of the perovskite material, C_{acc} is the capacitance formed as a result of the accumulation of ions at the interfaces formed by electron and hole transport materials and perovskite, and R_{iacc} modifies its resistivity depending on the accumulated ions at interface.

A diode is used in parallel with $R_{i,acc}$ representing the asymmetric charging and discharging of the interface, leading to easy capture of ionic charges at the interface. One of the reasons for this asymmetric behavior could be the accumulation of anions and cations, so that in equilibrium in the dark, anions accumulate at the interface with Spiro-MeOTAD and cations accumulate at the interface of TiO_2, while in semi stable lighting conditions the reverse phenomenon occurs. This accumulation of ions at the interfaces gives the formation of a double ionic layer, and as a result the energy band bends. When the illumination is suppressed, the electrons in TiO_2 recombine with holes in the perovskite layer, a behavior that is illustrated in the rapid drop in photovoltage; as for the slow drop in photovoltage, this would depend on the decay of the internal ionic double layer, since it forms a potential barrier that prevents electrons and holes from returning to the perovskite material and recombining.

Reflecting that some effects introduce the immobilization of ions in the interface, the diffusion of ions through organic contact [38] and JV hysteresis have been attributed to mobile vacancies [25]. The varying concentration of $Cs_{0.05}FA_{1-X}MA_XPb(I_{1-X}Br_X)_3$ results in a perovskite layer that displays changes in the asymmetric contribution obtained in the photovoltage transient measurements in double and triple cation perovskite based solar devices. The values of the electronic and ionic components of each solar cell are adjusted accordingly.

3.3. Ion Migration Fitting in Photovoltage Measurements

In an ion migration analysis, an exponential and quadratic fitting of the open circuit voltage decay is adjusted to obtain the ion mobility in the perovskite layer. From this fitting, a polynomial dependency on the V_{oc} and the diffusion time (t_d) is obtained; in turn, the diffusion time provides the required information to obtain the drift speed (v_d), which is the average speed reached by charged particles (ions, electrons, or holes) in a material due

to an electric field [39]. Since the resistivity in a semiconductor material is proportional to the magnitude of the electric field; therefore, Ohm's law can be expressed in terms of drift speed with the expression [39]:

$$v_d = \mu E \tag{2}$$

where μ is the mobility of the particles and E is the electric field, which is generated between two charged parallel plates and is given by the expression [38]:

$$E = \frac{V}{L} \tag{3}$$

where V is the potential difference existing between the plates and L is the thickness (m) formed by the two parallel plates. In addition, the drift speed (v_d) is obtained from the quotient of L and the diffusion time (t_d), the latter obtained from the exponential and quadratic fit of the asymmetric curve of the voltage decay in open circuit. In this way, combining Equations (1) and (2) we obtain the mobility of the particles in the expression:

$$\mu = \frac{L^2}{t_d V} \tag{4}$$

4. Results and Discussion

4.1. Morphological and Optical Characterization

Figure 3a,b show the transversal scanning electron microscope (SEM) image of the prepared sample. Analyzing the image by ImageJ software, the cross section obtained from an SEM of the sample with the configuration $Cs_{0.05}FA_{0.83}MA_{0.17}Pb(I_{0.83}Br_{0.17})_3$ is observed. From there, we can obtain the thicknesses of the thin films of the perovskite solar cell: FTO is 300 nm thickness, compact TiO_2 about 80 nm, mesoporous TiO_2 about 150 nm, perovskite layer thickness about 550 nm, spiro-MeOTAD about 100 nm and Au about 90 nm [40].
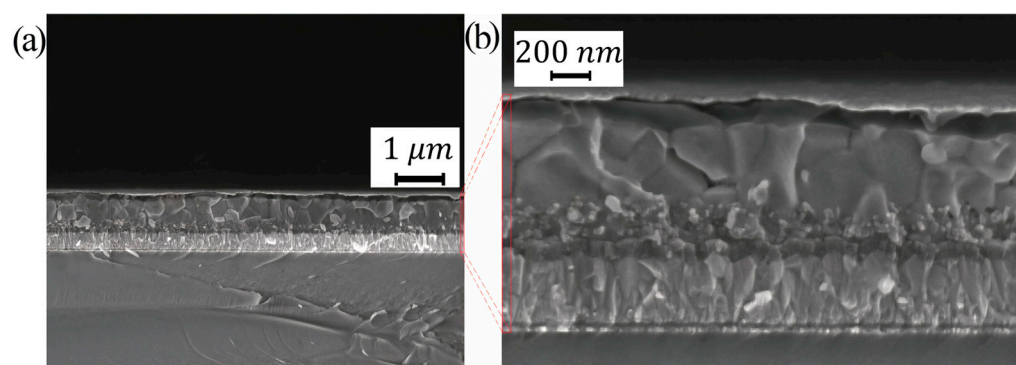
Figure 3. SEM images of the cross section of the control sample. (**a**) 1 μm; (**b**) 200 nm.

The determination of the composition of mixed cation perovskite films is very difficult. First, the thickness of the perovskite film is a few hundred nanometers, so there is only a small amount of material distributed on the film area. A further complication is the use of formamidinium and methylammonium in the film. Common elemental characterization techniques have atoms with low sensitivity to light (such as C, H, or N) [41]. Some reports on perovskite materials show the discrepancy between the solution and film compositions and indicate that the precursor solution and film obtained do not necessarily possess the same stoichiometry [41]. In practice, the formation of the perovskite materials is obtained by adding an amount of each material and obtaining the optical characterization of this material. The absorption spectra are shown in Figure 4. The absorption can increase if the thickness of the photoactive layer increases, although this was not so in our case, in which we had similar film thicknesses.
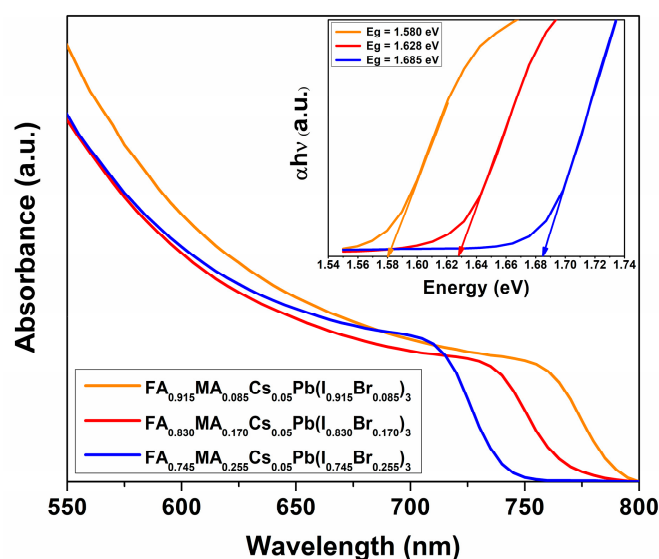
Figure 4. Absorption spectra of the samples under study.

For methylammonium perovskites [42–44] and formamidinium analogues [45], iodide was replaced by other halides, such as bromide [46]. This transition changes the band gap from approximately 1.5 to 2.3 eV. Moreover, it is also possible to simultaneously change the MA/FA and Br/I ratios [8,47,48] based on these mixed perovskites where the best cells have some of the iodine replaced with bromide and most of the MA replaced by FA. According to T. Jesper Jacobsson et al., a higher bromide content results in a higher band gap, which is true regardless of the FA/MA-ratio. The band gap is, however, not the only thing that changes as the shape of the absorption curve also changes with halide composition [49]. Therefore, in our devices, the higher concentration for FAPbI3 reduces the band gap in the materials and the reduction of the band gap increases the absorption spectra (see the Figure 4), leading to the enhancement of the absorption spectra which increases the Jsc [50–52].

4.2. Current Density–Voltage (J–V)

Figure 5 shows the J–V curves of the perovskite for the samples with the configurations: $Cs_{0.05}FA_{0.915}MA_{0.085}Pb(I_{0.915}Br_{0.085})_3$, $Cs_{0.05}FA_{0.83}MA_{0.17}Pb(I_{0.83}Br_{0.17})_3$ and $Cs_{0.05}FA_{0.745}MA_{0.255}Pb(I_{0.745}Br_{0.255})_3$. The control device (sample named 0.83) delivers a PCE of 12.1% with an open circuit voltage (V_{oc}) of 1.113 V, a short circuit current (J_{sc}) of 18.90 mA/cm^2 and a fill factor (FF) of 57.7%. When a greater amount of FA$^+$ is added at 0.915 to perovskite, the PCE increases to 14.0%; and when the FA$^+$ amount is 0.745 in perovskite, the PCE decreases to 11.54% (Table 1). The improved performance of the device with 0.915 FA$^+$ could be attributed to the improved quality of the perovskite film upon deposition. The enhancement of J$_{sc}$ by the enlarged absorption spectra (see Figure 4) and another possible reason for this increase in PCE would be that the multi cation perovskite results in a stabilized crystal structure [15]. In comparing the two, the ionic size of FA$^+$ (radius = 2.79 Å) is greater than that of MA$^+$ (radius = 2.70 Å). Moreover, the formation of hydrogen bonds between the H atoms in the C of the methyl group in $CH_3NH_3^+$ and the surrounding halides in the octahedrons metal halide can contribute to stabilize the lattice; on the other hand, a strong electrostatic interaction of Cs$^+$ (radius = 1.81 Å) with Br$^-$ and I$^-$ stabilizes the crystal structure [15]. The photoconversion efficiency obtained depends on the physical parameters of the device. For example, high efficiency is obtained using multiples cations and halides with tunable light absorption. Humidity, oxygen, and temperature are the main factors which limit the efficiency.
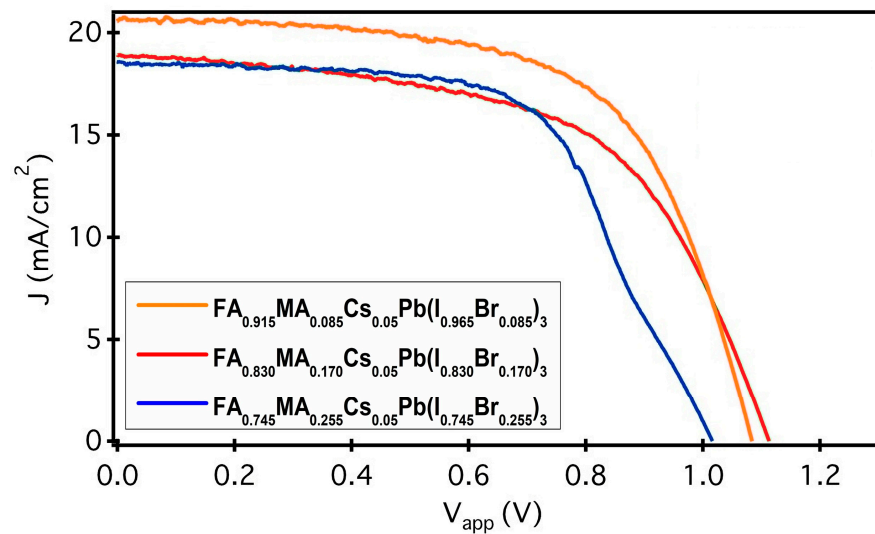
Figure 5.　J–V curves of solar cells with different concentrations, composed of $Cs_{0.05}FA_{1-X}MA_XPb(I_{1-X}Br_X)_3$.

Table 1. Summary of the photovoltaic parameters of solar cells with different concentrations, composed of $Cs_{0.05}FA_{1-X}MA_XPb(I_{1-X}Br_X)_3$.

Sample	Jsc (mA/cm^2)	V_{oc} (V)	FF (%)	η (%)
0.915	20.60	1.084	62.50	14.00
0.83	18.90	1.113	57.70	12.10
0.745	18.56	1.016	61.16	11.54

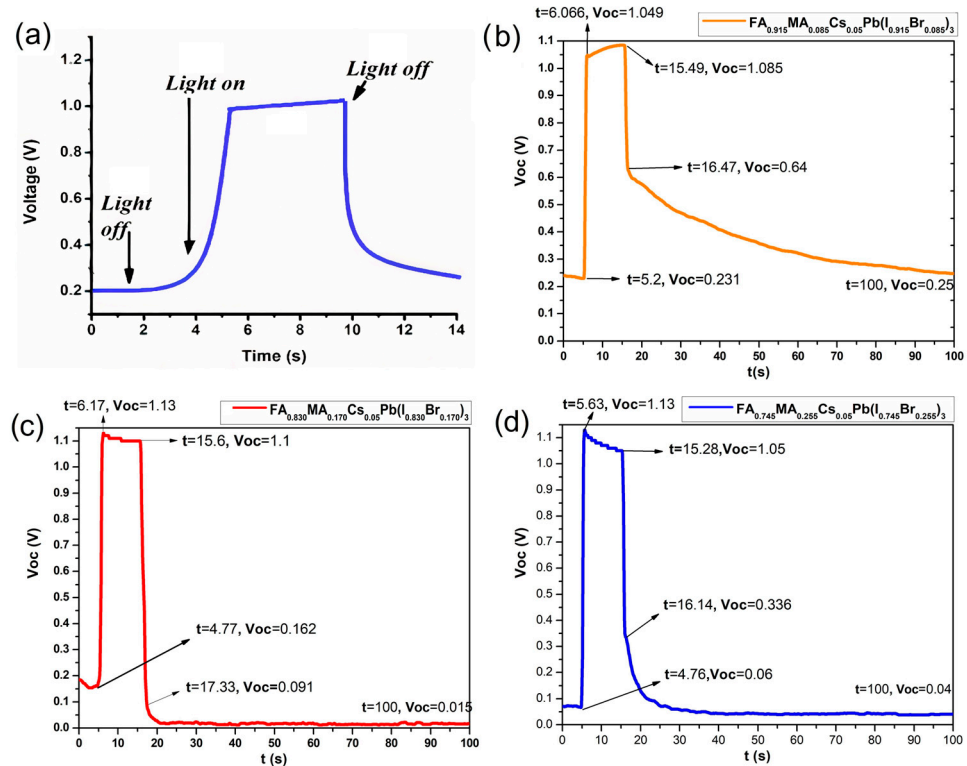*4.3. OCVD Measurements*

The OCVD measurement was made through the excitation of the device with a 100 mW/cm^2 lamp in the devices composed of $Cs_{0.05}FA_{1-X}MA_XPb(I_{1-X}Br_X)_3$ with an area of 0.16 cm^2. The photocharge and discharge transient processes and their behavior under different concentrations in the precursor are observed in Figure 6.

To understand the process of OCVD measurements, we will use a diagram as illustrated in Figure 6a. Figure 6b shows the solar cell in equilibrium in darkness. When the device is illuminated, a rapid increase in voltage is generated which we will call ΔV R1. Figure 6c shows that after some time in lighting equilibrium, a slow increase is detected, ΔV R2. Figure 6d shows that when the light is suppressed, there are two photovoltage decays, one fast ΔV D1 and the other one slow ΔV D2; the photovoltage decrease profile of the devices indicates at first glance that it does not have the symmetrical behavior that is common for other types of solar cells [30].

Table 2 shows a summary of the photovoltage increases and decreases for all types of solar cells under consideration. The initial rapid rise leads to gaining a major portion of the open circuit voltage ΔV R1, (ΔV R1 = 1.07 mV) for the sample named 0.915, within 90 ms of turning on the light, followed by a small increase in potential (ΔV R2 = 0.36 mV) with a slowly rising profile in $τ_{r1}$ = 9.42 s. The rapid fall leads to great loss of V_{oc} (ΔV D1 = 0.445 mV) in less than 98 ms after turning off the light, which is followed by a slow decay (ΔV D2 = 0.39 mV) after only a few tens of seconds ($τ_{d2}$). As shown in Figure 6b, the slow increase could be due to a better crystallization of perovskite in its combination of 0.915 of FA$^+$ and 0.085 of MA$^+$. These percentages would improve the charge transport and slow the ionic kinetics. Likewise, at the moment of suppressing the light, the device goes into the dark process rapidly around 0.64 V, where the ionic movementchanges direction, until reaching the dark equilibrium again.

Figure 6. (**a**) OCVD measurements diagram for profiles with different concentrations of (**b**) $Cs_{0.05}FA_{0.915}MA_{0.085}Pb(I_{0.915}Br_{0.085})_3$ (**c**) $Cs_{0.05}FA_{0.83}MA_{0.17}Pb(I_{0.83}Br_{0.17})_3$ and (**d**) $Cs_{0.05}FA_{0.745}MA_{0.255}Pb(I_{0.745}Br_{0.255})_3$.

Table 2. Summary of the photovoltaic parameters of solar cells with different concentrations composed of $Cs_{0.05}FA_{1-X}MA_XPb(I_{1-X}Br_X)_3$.

FAI	Rapid Increase		Slow Increase		Fast Decay		Slow Decay	
M	ΔVR1 (V)	τ_{r1} (ms)	ΔVR2 (V)	τ_{r2} (s)	ΔVD1 (V)	τ_{d1} (ms)	ΔVD2 (V)	τ_{d2} (s)
1.135	1.07	90	0.36	9.42	0.445	98	0.39	83.53
1.03	0.968	140	0.03	9.43	1.009	173	0.076	82.67
0.924	0.817	90	0.08	9.65	0.714	86	0.296	83.86

Several studies show that the incorporation of MA^+ cation in the $FAPbI_3$ cation increases the photoconversion efficiency in solar cells [53,54]. The FA^+ cation has an estimated ionic radius of about 2.2 Å which is higher than the estimated ionic radius of MA^+ cation of about 1.8 Å. The introduction of FA^+ reduces the band gap which in turn increases the absorption spectra (810 nm, see Figure 4) [15,55]. The $MA_xFA_{1-x}PbI_3$ structure improves the stability of the film, thereby overcoming the instability of the $FAPbI_3$ phase at ambient temperature [48,56]. $FAPbI_3$ has two phases, the black phase, α-$FAPbI_3$ [57], and the yellow phase, δ-$FAPbI_3$ [58]. At ambient temperature, the black phase can change to yellow phase in a change associated with crystallization [59,60]. On the other hand, an increase in grain size of the perovskite film helps to reduce the recombination of charge carriers by decreasing the total grain boundary area. Evidence of this was supported by transient photovoltage results [61].

For the 0.83 device, the initial rapid rise gains a major portion of open circuit voltage ΔV R1 (ΔV R1 = 0.968 mV) within 140 ms of turning on the light, followed by a small decrease in potential (ΔV R2 = −0.03 mV) with a slowly rising profile in τ_{r2} = 9.43 s. The rapid decay leads to a large loss of V_{oc} (ΔV D1 = 1.009 mV) in less than 173 ms after turning off the light, followed by a slow decay (ΔV D2 = 0.076 mV) after only a few tens of a second (τ_{d2}). As shown in Figure 6c, the slow decrease could be due to crystallization

of perovskite and the size of the crystals in their combination of 0.83 of FA$^+$ and 0.17 of MA$^+$, in such a way that the ionic movement would accelerate. This could generate charge recombination while the device is illuminated and at the moment of suppressing the light, the ionic movement would change direction drastically which would reach a relaxation in the dark close to 0.091 V.

For the case of the 0.745 sample device, the initial rapid rise gains a major portion of open circuit voltage ΔV R1 (ΔV R1 = 0.817 mV) within 90 ms of turning on the light, followed by a small decrease in potential (ΔV R2 = −0.08 mV) with a slowly rising profile in τ_{r2} = 9.65 s. The rapid fall leads to great loss of V$_{oc}$ (ΔV D1 = 0.714 mV) and the fast decay leads to large loss of power in less than 86 ms after the light is turned off, which is followed by slow decay (ΔV D2 = 0.296 mV) after only a few tens of a seconds (τ_{d2}). As shown in Figure 6d, similarly to the device with 0.83 of FA$^+$, the slow decrease could be due to crystallization of perovskite. Enhancing the amount of MA$^+$ in perovskite could change the ionic movement near 0.336 V until it reaches its equilibrium in darkness.

4.4. Equivalent Circuit in PSpice

As illustrated in Figure 2, two parallel parts have been considered in the equivalent circuit proposed by F. Ebadi et al. [30]: one for the ionic process, and the other represents the equivalent electrical components related to common electronic processes. The recombination resistance (R$_{rec}$) of free charge carriers can be obtained from the electronic branch of the equivalent circuit. By adjusting the passive component values and by comparing the simulated versus the experimental curves for each perovskite layer concentration as shown in Figure 7, the values can be obtained. Table 3 summarizes the passive elements of the equivalent circuit.
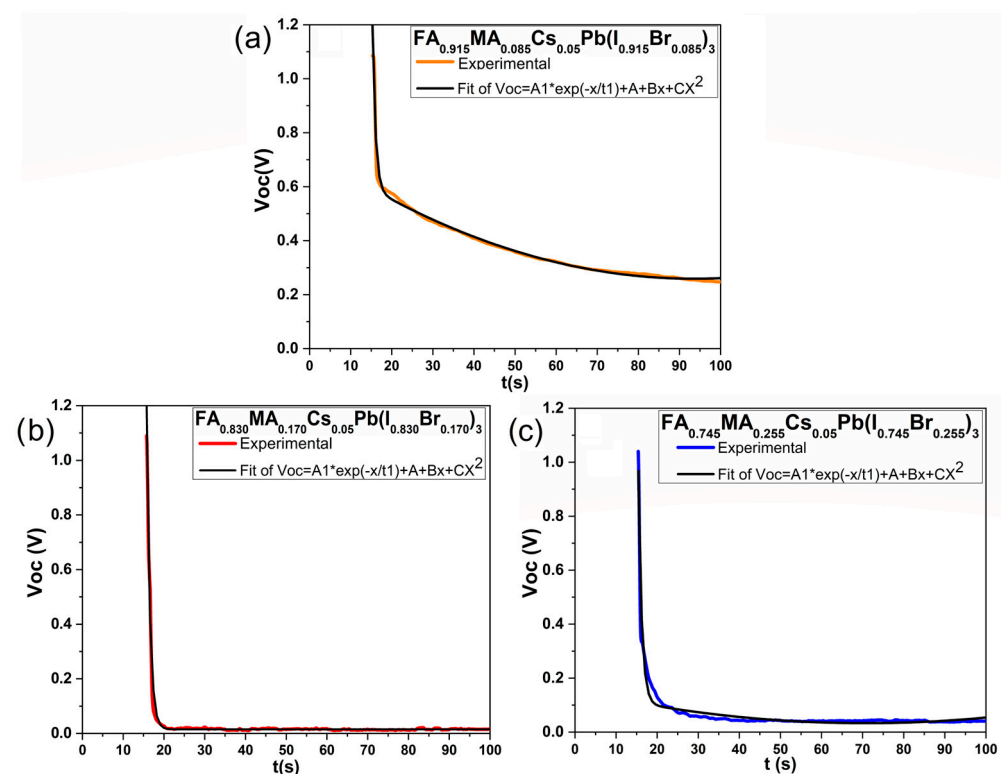
Figure 7. Simulation and profile of increase and decrease of photovoltage of solar cells based on the various concentrations of (**a**) Cs$_{0.05}$FA$_{0.915}$MA$_{0.085}$Pb(I$_{0.915}$ Br$_{0.085}$)$_3$, (**b**) Cs$_{0.05}$FA$_{0.83}$MA$_{0.17}$Pb(I$_{0.83}$Br$_{0.17}$)$_3$ and (**c**) Cs$_{0.05}$FA$_{0.745}$MA$_{0.255}$Pb(I$_{0.745}$Br$_{0.255}$)$_3$.

Table 3. Values of the passive elements of the equivalent circuit with various concentrations of $Cs_{0.05}FA_{1-X}MA_XPb(I_{1-X}Br_X)_3$.

FAI	R_{rec}	R_t	C_{bulk}	$R_{i,bulk}$	$R_{i,acc}$	C_{acc}
M	Ωcm^2	Ωcm^2	Fcm^2	Ωcm^2	Ωcm^2	Fcm^2
1.135 M	2.54×10^{12}	0.50×10^9	3.99×10^{-2}	25×10^9	25.0×10^9	1.56×10^{-3}
1.03 M	8.8×10^8	1.00×10^3	7.18×10^{-1}	50×10^3	50.0×10^3	5.31×10^{-2}
0.924 M	1.84×10^5	0.50×10^3	8.75×10^{-5}	15×10^3	75.0×10^3	4.96×10^{-2}

4.5. Ion Mobility Fitting

In the ion mobility study, exponential and quadratic adjustments were made to the photovoltaic decay curves, as seen in Figure 7. From the exponential adjustments, polynomials dependent on V_{oc} and diffusion time (t_d) of each FA^+ concentration, and the thickness of the perovskite film ($\sim$550 nm) adjustments were obtained according to Equation (1). In Figure 7, the exponential and quadratic fit for the different concentrations of FA^+ are observed, where the coefficient of determination (Adj. R-Square) for the sample 0.915 is 0.988, for the sample 0.83 is 0.983, and for the sample 0.745 is 0.942.

For the sample 0.915 in Figure 7a, when V_{oc} is at its maximum value (1.085 V) a diffusion coefficient of 4.24×10^{-12} cm^2/s is recorded, and in the rapid decay of V_{oc} (ΔV D1) up to 0.64 V, the diffusion coefficient increases exponentially up to 7.45×10^{-12} cm^2/s. This little change of 3.21×10^{-12} cm^2/s could be due to the fact that free charge recombination processes mostly occur in the rapid decay of V_{oc}, and in this period of time the movement of MA^+ ions in cubic phase would be recorded as shown by Futscher et al. [62] with a diffusion coefficient of 6.8×10^{-12} cm^2/s. When the device begins to relax in darkness, the photovoltage slowly drops down to 0.25 V, and the diffusion coefficients show a quadratic drop down to 3.26×10^{-12} cm^2/s, where the movement of MA^+ ions in the tetragonal phase is recorded with a diffusion coefficient of 3.4×10^{-12} cm^2/s. With this method, we could not detect the movement of the ions of I^- (3.1×10^{-09} cm^2/s) [62], since the slower ion would somehow slow down the kinetics of the other ions (FA^+, I^-, Br^-), with the movement of MA^+ ions being predominant.

For the 0.83 sample in Figure 7b, when the V_{oc} is at its maximum value (1.1 V) a diffusion coefficient 4.08×10^{-12} cm^2/s is recorded, and in the rapid decay of V_{oc} (ΔV D1) up to 0.009 V, the diffusion coefficient increases exponentially up to 5.6×10^{-11} cm^2/s. This change in diffusion coefficients could be due to the concentration of FA^+ and MA^+, and to associated accelerated ionic kinetics. When it begins to relax in darkness, the photovoltage slowly drops from 0.09 V to 0.015 V, and the diffusion coefficient reaches a maximum value of 2.26×10^{-10} cm^2/s. Here, the faster ions (I^-) are probably pushing the slower ones, averaging the kinetics of all the ions; and when the device is in the equilibrium state (0.015 V), a diffusion coefficient of 5.36×10^{-11} cm^2/s is recorded.

Similarly, for the sample named 0.745 in Figure 7c, when the V_{oc} is at its maximum value (1.016 V), a diffusion coefficient 5.25×10^{-12} cm^2/s is recorded. In the rapid decay of V_{oc} (ΔV D1) up to 0.33 V, the diffusion coefficient shows an exponential increase up to 1.56×10^{-11} cm^2/s. From here, the slow photovoltage decay begins and the highest diffusion coefficient was recorded at 3.95×10^{-11} cm^2/s with a voltage of 0.096 V. There was an oscillatory decrease in the diffusion coefficient until it reached a value of 3.37×10^{-11} cm^2/s.

It is useful to make a comparison with the devices made by Monojit Bag et al. [63], whose devices were manufactured with $MAPbI_3$, $MA_xFA_{1-x}PbI_3$ and $FAPbI_3$, and a perovskite film thickness of 300 nm at 318 K, for which diffusion coefficients of 3.6×10^{-12} cm^2/s, 2.0×10^{-12} cm^2/s, and 3.0×10^{-12} cm^2/s were obtained, respectively. To obtain the diffusion coefficients, the Einstein–Smoluchowski relationship is used: $D = \mu((k_BT)/q)$, where D is the diffusion coefficient, μ the mobility of the particle, k_B the Boltzmann constant, T the absolute temperature and q the elemental charge (Table 4).

Table 4. Diffusion coefficients of solar cells based on various concentrations of $Cs_{0.05}FA_{1-X}MA_XPb(I_{1-X}Br_X)_3$.

FAI (M)	Voc Max (V)	D (cm^2/s)	ΔVD1 (V)	D (cm^2/s)	Voc Min (V)	D (cm^2/s)
1.135	1.084	4.24×10^{-12}	0.64	7.45×10^{-12}	0.25	3.26×10^{-12}
1.03	1.113	4.08×10^{-12}	0.009	5.6×10^{-11}	0.015	2.26×10^{-10}
0.924	1.016	5.25×10^{-12}	0.33	1.56×10^{-11}	0.096	3.95×10^{-11}

If we compare the diffusion coefficients of the sample named 0.83, which is the control sample with a range of 10^{-10} to 10^{-12} cm^2/s, with the device $MA_xFA_{1-x}PbI_3$ from Monojit of 2.0×10^{-12} cm^2/s, our devices are in the same range (see Figure 8); the difference in value could be due to different factors such as the perovskite thin film thickness and measurement temperature among many others.
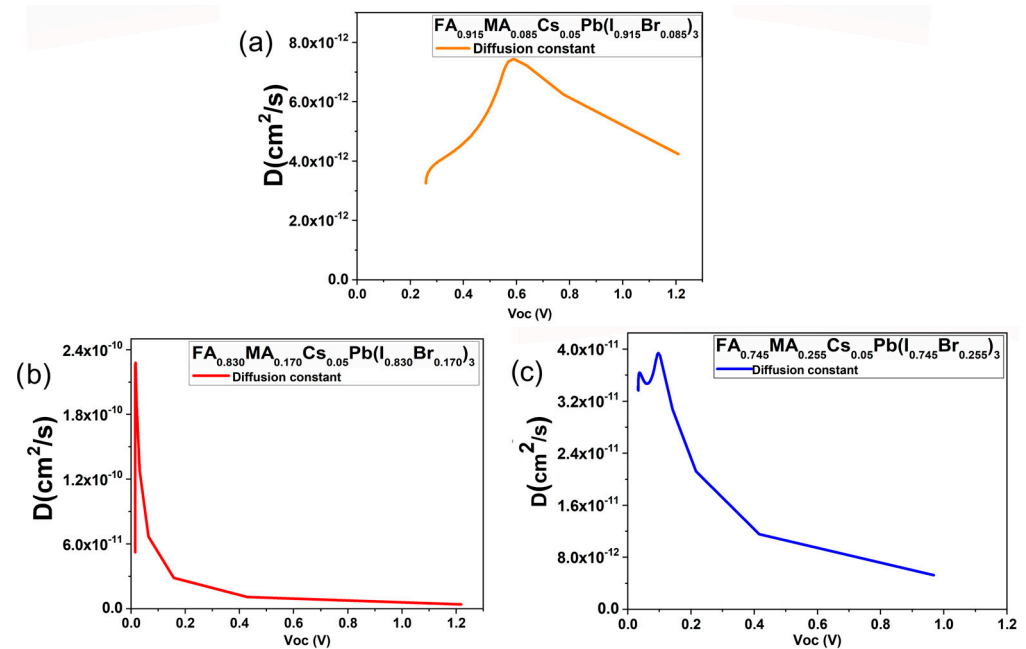
Figure 8. Voltage dependent diffusion coefficients of solar cells with concentrations of (**a**) $Cs_{0.05}FA_{0.915}MA_{0.085}Pb(I_{0.915}$ $Br_{0.085})_3$, (**b**) $Cs_{0.05}FA_{0.83}$ $MA_{0.17}Pb(I_{0.83}Br_{0.17})_3$ and (**c**) $Cs_{0.05}FA_{0.745}MA_{0.255}Pb(I_{0.745}Br_{0.255})_3$.

As seen in Figure 8c, in our cell, with concentration $FAPbI_3$ (0.915), at the moment of light suppression, the ions exhibited an ionic diffusion coefficient of 4.24×10^{-12} cm^2/s for 90 ns. This corresponds to a rapid time decay of Voc. An acceleration to 7.45×10^{-12} cm^2/s immediately occurs at a voltage of 0.68 V. As the sample reaches its relaxed state, the ions have an exponential deceleration for 100 s of 3.26×10^{-12} cm^2/s at a voltage of 0.25 V. This indicates that the ions still need more time to reach their relaxation state. The devices with $FAPbI_3$ (0.83) and $FAPbI_3$ (0.745) show ionic diffusion coefficients of 4.08×10^{-12} cm^2/s and 5.25×10^{-12} cm^2/s, respectively. These devices accelerate up to about 5.60×10^{-11} cm^2/s and 1.56×10^{-11} cm^2/s, respectively, and are closer to their relaxed state. This behavior could be due to changes in the electrostatic potential linked to ionic redistribution that controls the local concentration of electrons and holes in the perovskite. This is critical because the concentration of free electrons at the perovskite/spiro interface and the concentration of holes at the TiO_2/perovskite interface delimits the recombination rate via interfacial traps to the respective populations of holes and electrons in the HTM and ETM layers. Thus, the electrostatic potential profile due to ionic charge

controls the rate of recombination of holes and electrons at the interfaces, and this in turn controls the current-voltage characteristics of the device [23].

In addition, the samples FAPbI3 (0.83) and FAPbI3 (0.745) show a recombination resistance of about 8.8×10^8 $\Omega \cdot cm^2$ and 1.84×10^5 $\Omega \cdot cm^2$, respectively. These values show that these samples have a higher recombination rate, and that they are less efficient devices than the sample FAPbI3 (0.915). Finally, it is worth mentioning that their bulk and ionic capacitances are too large and exceed those of the real ones in perovskite solar cells since our experimental curves, while they are illuminated, exhibit irregularities (increase/decrease) and the simulated curves remain constant, which gives complexity to the numerical simulations.

Ion migration has been recognized as a phenomenon of great importance describing the kinetic response of perovskite solar cells [64,65] with direct observations of compositional changes [66,67], and a large capacitance observed in measurements in darkness. This capacitance has been interpreted as a Helmholtz capacitance caused by the accumulation of ions [68,69]. In the results of the proposed equivalent circuit for the device with the concentration of FAPbI3 (0.915), large capacitances are observed with orders of magnitude of $>10^{-2}$ $F \cdot cm^{-2}$ and $>10^{-3}$ $F \cdot cm^{-2}$ for bulk and ionic, respectively. Similar capacitances were also reported in works in which the equivalent circuit simulations resulted in high capacitive effects ($>10^{-3}$ $F \cdot cm^{-2}$) [70–74]. Bisquert et al. proposed that giant capacitances and inductances arise from the accumulation or release of phase-shifted electronic charge from inside a degenerate layer induced by fluctuations in surface polarization due to ionic charge [71,75]. Christopher Eames in 2015 reported the activation energies for the ions of 0.58 eV for Iodine (I^-) and 0.84 eV for MA^+, and yet in 2019 Moritz H. Futscher reported that the activation energies are 0.29 eV for Iodine (I^-) and 0.39 eV for MA^+ in cubic phase and 0.90 eV in tetragonal phase, so the activation energies vary depending on the composition of the perovskite as well as its structural phase, not to mention that the perovskite can count on other ions such as Br^- and FA^+.

In addition, the FAPbI3 (0.915) devices showed a recombination resistance of Rrec = 2.54×10^{12} $\Omega \cdot cm^2$, which is four and seven times higher than the samples FAPbI3 (0.83) and FAPbI3 (0.745), respectively. Thus FAPbI3 (0.915) samples showed considerable improvement. This phenomenon is due to the internal electric field that is a driving force for charge redistribution in the solar cell, inducing energy band alignment [22]. Alignment of Fermi levels in different layers that compose the device promotes the accumulation of positive charge at the TiO_2/perovskite interface leading to unwanted recombination of mobile charge carriers as reported by Matyas Daboczi et al. [22]. When illumination is suppressed, a slow decay of Voc occurs. This slow decay may be related to the low electron density in the perovskite due to the rapid electron transfer to TiO_2 and, at the same time, to the hole-blocking property of the perovskite film [22].

5. Conclusions

In conclusion, the study is based on obtaining the resistance to recombination of mobile charge carriers and ionic migration in perovskite solar cells, by means of a luminous pulse in open circuit voltage (Voc), from which an asymmetric rise and decay of Voc is obtained. From the curves drawn, the parameters of an equivalent circuit can be obtained by simulating the experimental curves. With this method, the solar cell does not suffer as much deterioration as with the impedance spectroscopy method, and the characterization is much simpler and faster to achieve. Therefore, it can be confirmed that the samples $Cs_{0.05}FA_{0.745}MA_{0.255}Pb(I_{0.745}Br_{0.255})_3$ and $Cs_{0.05}FA_{0.83}MA_{0.17}Pb(I_{0.83}Br_{0.17})_3$ show a resistance to recombination of 1.84×10^5 Ωcm^2 and 8.8×10^8 Ωcm^2, respectively, so they have a higher recombination rate and are less efficient devices than the sample $Cs_{0.05}FA_{0.915}MA_{0.085}Pb(I_{0.915}Br_{0.085})_3$ with its rate of 2.54×10^{12} Ωcm^2. In addition, with the open voltage drops (Voc) the ionic diffusion coefficients can be obtained for each Voc point, without the need for activation energy, a characterization that requires different temperatures from which the cell may suffer degradation. Therefore, from the quadratic

and exponential fittings of the open circuit voltage decay, the ionic diffusion coefficients can be obtained in ranges close to those in the literature; however, with this method the specific ion cannot be known.

References

1. Almora, O.; Baran, D.; Bazan, G.C.; Berger, C.; Cabrera, C.I.; Catchpole, K.R.; Erten-Ela, S.; Guo, F.; Hauch, J.; Ho-Baillie, A.W.Y.; et al. Device performance of emerging photovoltaic materials (version 1). *Adv. Energy Mater.* **2021**, *11*, 2002774. [CrossRef]
2. Stranks, S.D.; Eperon, G.E.; Grancini, G.; Menelaou, C.; Alcocer, M.J.P.; Leijtens, T.; Herz, L.M.; Petrozza, A.; Snaith, H.J. Electron-hole diffusion lengths exceeding 1 micrometer in an organometal trihalide perovskite absorber. *Science* **2013**, *342*, 341–344. [CrossRef] [PubMed]
3. Wang, P.; Wu, Y.; Cai, B.; Ma, Q.; Zheng, X.; Zhang, W.H. Solution- Processable Perovskite Solar Cells toward Commercialization: Progress and Challenges. *Adv. Funct. Mater.* **2019**, *29*, 1807661. [CrossRef]
4. D'Innocenzo, V.; Kandada, A.R.S.; De Bastiani, M.; Gandini, M.; Petrozza, A. Tuning the light emission properties by band gap engineering in hybrid lead halide perovskite. *J. Am. Chem. Soc.* **2014**, *136*, 17730–17733. [CrossRef]
5. Wang, R.; Mujahid, M.; Duan, Y.; Wang, Z.K.; Xue, J.; Yang, Y. A review of perovskites solar cell stability. *Adv. Funct. Mater.* **2019**, *29*, 1808843. [CrossRef]
6. Yang, W.S.; Park, B.-W.; Jung, E.H.; Jeon, N.J.; Kim, Y.C.; Lee, D.U.; Shin, S.S.; Seo, J.; Kim, E.K.; Seok, J.H.N.A.I. Iodide management in formamidinium-lead-halide–based perovskite layers for efficient solar cells. *Science* **2019**, *356*, 1376–1379. [CrossRef]
7. Bi, D.; Tress, W.; Dar, M.I.; Gao, P.; Luo, J.; Renevier, C.; Schenk, K.; Abate, A.; Giordano, F.; Baena, J.-P.C.; et al. Efficient luminescent solar cells based on tailored mixed-cation perovskites. *Sci. Adv.* **2016**, *2*, e1501170. [CrossRef]
8. Baena, J.P.C.; Steier, L.; Tress, W.; Saliba, M.; Neutzner, S.; Matsui, T.; Giordano, F.; Jacobsson, T.J.; Kandada, A.R.S.; Zakeeruddin, S.M.; et al. Highly efficient planar perovskite solar cells through band alignment engineering. *Energy Environ. Sci.* **2015**, *8*, 2928–2934. [CrossRef]
9. Saliba, M.; Matsui, T.; Seo, J.-Y.; Domanski, K.; Correa-Baena, J.-P.; Nazeeruddin, M.K.; Zakeeruddin, S.M.; Tress, W.; Abate, A.; Hagfeldt, A.; et al. Cesium-containing triple cation perovskite solar cells: Improved stability, reproducibility and high efficiency. *Energy Environ. Sci.* **2016**, *9*, 1989–1997. [CrossRef]
10. Saliba, M.; Matsui, T.; Domanski, K.; Seo, J.-Y.; Ummadisingu, A.; Zakeeruddin, S.M.; Correa-Baena, J.-P.; Tress, W.; Abate, A.; Hagfeldt, A.; et al. Incorporation of rubidium cations into perovskite solar cells improves photovoltaic performance. *Science* **2016**, *354*, 206–209. [CrossRef]
11. Torres, J.; Sanchez-Diaz, J.; Rivas, J.M.; de la Torre, J.; Zarazua, I.; Esparza, D. Electrical properties and JV modeling of perovskite (CH$_3$NH$_3$PbI$_3$) solar cells after external thermal exposure. *Sol. Energy* **2021**, *222*, 95–102. [CrossRef]
12. Xing, G.; Mathews, N.; Sun, S.; Lim, S.S.; Lam, Y.M.; Gr, M.; Mhaisalkar, S.; Sum, T.C. Long-range balanced electron-and hole-transport lengths in organic-inorganic CH$_3$NH$_3$PbI$_3$. *Science* **2013**, *342*, 344–347. [CrossRef] [PubMed]
13. Steirer, K.X.; Schulz, P.; Teeter, G.; Stevanovic, V.; Yang, M.; Zhu, K.; Berry, J.J. Defect tolerance in methylammonium lead triiodide perovskite. *ACS Energy Lett.* **2016**, *1*, 360–366. [CrossRef]
14. Yin, W.-J.; Shi, T.; Yan, Y. Unusual defect physics in CH3NH3PbI3 perovskite solar cell absorber. *Appl. Phys. Lett.* **2014**, *104*, 063903. [CrossRef]
15. Kojima, A.; Teshima, K.; Shirai, Y.; Miyasaka, T. Organometal halide perovskites as visible-light sensitizers for photovoltaic cells. *J. Am. Chem. Soc.* **2009**, *131*, 6050–6051. [CrossRef]
16. Polman, A.; Knight, M.; Garnett, E.C.; Ehrler, B.; Sinke, W.C. Photovoltaic materials: Present efficiencies and future challenges. *Science* **2016**, *352*, aad4424. [CrossRef]
17. Jiang, Q.; Chu, Z.; Wang, P.; Yang, X.; Liu, H.; Wang, Y.; Yin, Z.; Wu, J.; Zhang, X.; You, J. Planar-structure perovskite solar cells with efficiency beyond 21%. *Adv. Mater.* **2017**, *29*, 1703852. [CrossRef]

18. Snaith, H.J.; Abate, A.; Ball, J.M.; Eperon, G.E.; Leijtens, T.; Noel, N.K.; Stranks, S.D.; Wang, J.T.-W.; Wojciechowski, K.; Zhang, W. Anomalous hysteresis in perovskite solar cells. *J. Phys. Chem. Lett.* **2014**, *5*, 1511–1515. [CrossRef]

19. Nandal, V.; Nair, P.R. Predictive modeling of ion migration induced degradation in perovskite solar cells. *ACS Nano* **2017**, *11*, 11505–11512. [CrossRef]

20. Bowring, A.R.; Bertoluzzi, L.; O'Regan, B.C.; McGehee, M.D. Reverse bias behavior of halide perovskite solar cells. *Adv. Energy Mater.* **2018**, *8*, 1702365. [CrossRef]

21. Gottesman, R.; Lopez-Varo, P.; Gouda, L.; Jimenez-Tejada, J.A.; Hu, J.; Tirosh, S.; Zaban, A.; Bisquert, J. Dynamic phenomena at perovskite/electron-selective contact interface as interpreted from photovoltage decays. *Chem* **2016**, *1*, 776–789. [CrossRef]

22. Daboczi, M.; Hamilton, I.; Xu, S.; Luke, J.; Limbu, S.; Lee, J.; McLachlan, M.A.; Lee, K.; Durrant, J.R.; Baikie, I.D.; et al. Origin of open-circuit voltage losses in perovskite solar cells investigated by surface photovoltage measurement. *ACS Appl. Mater. Interfaces* **2019**, *11*, 46808–46817. [CrossRef] [PubMed]

23. Moia, D.; Gelmetti, I.; Calado, P.; Fisher, W.; Stringer, M.; Game, O.; Hu, Y.; Docampo, P.; Lidzey, D.; Palomares, E.; et al. Ionic-to-electronic current amplification in hybrid perovskite solar cells: Ionically gated transistor-interface circuit model explains hysteresis and impedance of mixed conducting devices. *Energy Environ. Sci.* **2019**, *12*, 1296–1308. [CrossRef]

24. Belisle, R.A.; Nguyen, W.H.; Bowring, A.R.; Calado, P.; Li, X.; Irvine, S.J.C.; McGehee, M.D.; Barnes, P.R.F.; O'Regan, B.C. Interpretation of inverted photocurrent transients in organic lead halide perovskite solar cells: Proof of the field screening by mobile ions and determination of the space charge layer widths. *Energy Environ. Sci.* **2017**, *10*, 192–204. [CrossRef]

25. Tress, W.; Marinova, N.; Moehl, T.; Zakeeruddin, S.M.; Nazeeruddin, M.K.; Gr, M. Understanding the rate-dependent J–V hysteresis; slow time component, and aging in $CH_3NH_3PbI_3$ perovskite solar cells: The role of a compensated electric field. *Energy Environ. Sci.* **2015**, *8*, 995–1004. [CrossRef]

26. Eames, C.; Frost, J.M.; Barnes, P.R.; O'regan, B.C.; Walsh, A.; Islam, M.S. Ionic transport in hybrid lead iodide perovskite solar cells. *Nat. Commun.* **2015**, *6*, 1–8. [CrossRef]

27. Weber, S.A.L.; Hermes, I.M.; Gort, S.-H.T.-C.C.; Bergmann, V.W.; Gilson, L.; Hagfeldt, A.; Graetzel, M.; Tress, W.; Berger, R. How the formation of interfacial charge causes hysteresis in perovskite solar cells. *Energy Environ. Sci.* **2018**, *11*, 2404–2413. [CrossRef]

28. Calado, P.; Telford, A.M.; Bryant, D.; Li, X.; Nelson, J.; O'Regan, B.C.; Barnes, P.R.F. Evidence for ion migration in hybrid perovskite solar cells with minimal hysteresis. *Nat. Commun.* **2016**, *7*, 1–10. [CrossRef]

29. Frost, J.M.; Walsh, A. What is moving in hybrid halide perovskite solar cells? *Acc. Chem. Res.* **2016**, *49*, 528–535. [CrossRef]

30. Ebadi, F.; Aryanpour, M.; Mohammadpour, R.; Taghavinia, N. Coupled ionic-electronic equivalent circuit to describe asymmetric rise and decay of photovoltage profile in perovskite solar cells. *Sci. Rep.* **2019**, *9*, 1–9.

31. Zaban, A.; Greenshtein, M.; Bisquert, J. Determination of the electron lifetime in nanocrystalline dye solar cells by open-circuit voltage decay measurements. *ChemPhysChem* **2003**, *4*, 859–864. [CrossRef] [PubMed]

32. Baumann, A.; Tvingstedt, K.; Heiber, M.C.; Väth, S.; Momblona, C.; Bolink, H.J.; Dyakonov, V. Persistent photovoltage in methylammonium lead iodide perovskite solar cells. *Appl. Mater.* **2014**, *2*, 081501. [CrossRef]

33. Bertoluzzi, L.; Sanchez, R.S.; Liu, L.; Lee, J.-W.; Mas-Marza, E.; Han, H.; Park, N.-G.; Mora-Sero, I.; Bisquert, J. Cooperative kinetics of depolarization in CH 3 NH 3 PbI 3 perovskite solar cells. *Energy Environ. Sci.* **2015**, *2*, 910–915. [CrossRef]

34. Lopez-Varo, P.; Jim, J.A.; Garcıa-Rosell, M.; Ravishankar, S.; Garcia-Belmonte, G.; Bisquert, J.; Almora, O. Device physics of hybrid perovskite solar cells: Theory and experiment. *Adv. Energy Mater.* **2015**, *8*, 1702772. [CrossRef]

35. Wang, Q. Fast voltage decay in perovskite solar cells caused by depolarization of perovskite layer. *J. Phys. Chem. C* **2015**, *122*, 4822–4827. [CrossRef]

36. Sakhatskyi, K.; John, R.A.; Guerrero, A.; Tsarev, S.; Sabisch, S.; Das, T.; Matt, G.J.; Yakunin, S.; Cherniukh, I.; Kotyrba, M.; et al. Assessing the drawbacks and benefits of ion migration in lead Halide perovskites. *ACS Energy Lett.* **2022**, *7*, 3401–3414. [CrossRef]

37. Zhou, Y.; Zhou, Z.; Chen, M.; Zong, Y.; Huang, J.; Pang, S.; Padture, N.P. Doping and alloying for improved perovskite solar cells. *J. Mater. Chem. A* **2016**, *4*, 17623–17635. [CrossRef]

38. Guerrero, A.; You, J.; Aranda, C.; Kang, Y.S.; Garcia-Belmonte, G.; Zhou, H.; Bisquert, J.; Yang, Y. Interfacial degradation of planar lead halide perovskite solar cells. *ACS Nano* **2016**, *10*, 218–224. [CrossRef]

39. Griffiths, D.J. Introduction to electrodynamics, American Association of Physics Teachers. *Phys. Teach.* **2005**, *73*, 574.

40. Kim, H.P.; Yusoff, A.R.B.M.; Jang, J. Polystyrene enhanced crystallization of perovskites towards high performance solar cells. *Nanoscale Adv.* **2019**, *1*, 76–85. [CrossRef]

41. Pareja-Rivera, C.; Solis-Cambero, A.L.; Sanchez-Torres, M.; Lima, E.; Solis-Ibarra, D. On the true composition of mixed-cation perovskite films. *ACS Energy Lett.* **2018**, *3*, 2366–2367. [CrossRef]

42. Hoke, E.T.; Slotcavage, D.J.; Dohner, E.R.; Bowring, A.R.; Karunadasa, H.I.; McGehee, M.D. Reversible photo-induced trap formation in mixed-halide hybrid perovskites for photovoltaics. *Chem. Sci.* **2015**, *6*, 613–617. [CrossRef] [PubMed]

43. Aharon, S.; El Cohen, B.; Etgar, L. Hybrid lead halide iodide and lead halide bromide in efficient hole conductor free perovskite solar cell. *J. Phys. Chem. C* **2014**, *118*, 17160–17165. [CrossRef]

44. Sadhanala, A.; Deschler, F.; Thomas, T.H.; Dutton, S.E.; Goedel, K.C.; Hanusch, F.C.; Lai, M.L.; Steiner, U.; Bein, T.; Docampo, P.; et al. Preparation of single-phase films of CH3NH3Pb $(I_{1-x}Br_x)_3$ with sharp optical band edges. *J. Phys. Chem. Lett.* **2014**, *5*, 2501–2505. [CrossRef] [PubMed]

45. Eperon, G.E.; Stranks, S.D.; Menelaou, C.; Johnston, M.B.; Herz, L.M.; Snaith, H.J. Formamidinium lead trihalide: A broadly tunable perovskite for efficient planar heterojunction solar cells. *Energy Environ. Sci.* **2014**, *7*, 982–988. [CrossRef]

46. Heo, J.H.; Song, D.H.; Im, S.H. Planar CH$_3$NH$_3$PbBr$_3$ hybrid solar cells with 10.4% power conversion efficiency, fabricated by controlled crystallization in the spin-coating process. *Adv. Mater.* **2014**, *26*, 8179–8183. [CrossRef]
47. Yang, W.S.; Noh, J.H.; Jeon, N.J.; Kim, Y.C.; Ryu, S.; Seo, J.; Seok, S.I. High-performance photovoltaic perovskite layers fabricated through intramolecular exchange. *Science* **2015**, *348*, 1234–1237. [CrossRef]
48. Jeon, N.J.; Noh, J.H.; Yang, W.S.; Kim, Y.C.; Ryu, S.; Seo, J.; Seok, S.I. Compositional engineering of perovskite materials for high-performance solar cells. *Nature* **2015**, *517*, 476–480. [CrossRef]
49. Jacobsson, T.J.; Correa-Baena, J.P.; Pazoki, M.; Saliba, M.; Schenk, K.; Grätzel, M.; Hagfeldt, A. An exploration of the compositional space for mixed lead halogen perovskites for high efficiency solar cells. *Energy Environ. Sci.* **2016**, *9*, 1706–1724. [CrossRef]
50. Stanić, D.; Kojić, V.; Čižmar, T.; Juraić, K.; Bagladi, L.; Mangalam, J.; Rath, T.; Gajović, A. Simulating the Performance of a Formamidinium Based Mixed Cation Lead Halide Perovskite Solar Cell. *Materials* **2021**, *14*, 6341. [CrossRef]
51. Rai, M.; Wong, L.H.; Etgar, L. The Effect of the Perovskite Thickness on the Electroluminescence and Solar Cell Conversion Efficiency. *J. Phys. Chem. Lett.* **2020**, *11*, 8189–8194. [CrossRef] [PubMed]
52. Valle-Pulido, J.; Solis, O.E.; Esparza, D.; Rodriguez-Rojas, R.A.; Turren-Cruz, S.H.; Rivas, J.M.; Zarazua, I. Degradation analysis of perovskite solar cells doped with MABr3 via electrochemical impedance. *Sol. Energy* **2023**, *258*, 148–155. [CrossRef]
53. Zhou, Y.; Yang, M.; Pang, S.; Zhu, K.; Padture, N.P. Excep- tional morphology-preserving evolution of formamidinium lead triiodide perovskite thin films via organic-cation displacement. *J. Am. Chem. Soc.* **2016**, *138*, 5535–5538. [CrossRef]
54. Pellet, N.; Gao, P.; Gregori, G.; Yang, T.Y.; Nazeeruddin, M.K.; Maier, J.; Grätzel, M. Mixed-organic-cation Perovskite photovoltaics for enhanced solar-light harvesting. *Angew. Chem. Int. Ed.* **2014**, *53*, 3151–3157. [CrossRef] [PubMed]
55. Almora, O.; Baran, D.; Bazan, G.C.; Cabrera, C.I.; Erten-Ela, S.; Forberich, K.; Guo, F.; Hauch, J.; Ho-Baillie, A.W.Y.; Jacobsson, T.J.; et al. Device performance of emerging photovoltaic materials (Version 3). *Adv. Energy Mater.* **2023**, *13*, 2203313. [CrossRef]
56. Binek, A.; Hanusch, F.C.; Docampo, P.; Bein, T. Stabilization of the trigonal high-temperature phase of formamidinium lead iodide. *J. Phys. Chem. Lett.* **2015**, *6*, 1249–1253. [CrossRef]
57. Solis, O.E.; Fernandez-Saiz, C.; Rivas, J.M.; Esparza, D.; Turren-Cruz, S.H.; Julian-Lopez, B.; Boix, P.P.; Mora-Sero, I. α-FAPbI$_3$ powder presynthesized by microwave irradiation for photovoltaic applications. *Electrochim. Acta* **2023**, *439*, 141701. [CrossRef]
58. Weller, M.T.; Weber, O.J.; Frost, J.M.; Walsh, A. Cubic perovskite structure of black formamidinium lead iodide, α-[HC(NH$_2$)$_2$]PbI$_3$, at 298 K. *J. Phys. Chem. Lett.* **2015**, *6*, 3209–3212. [CrossRef]
59. Wang, Z.; Zhou, Y.; Pang, S.; Xiao, Z.; Zhang, J.; Chai, W.; Xu, H.; Liu, Z.; Padture, N.P.; Cui, G. Additive-modulated evolution of HC (NH2) 2PbI3 black polymorph for mesoscopic perovskite solar cells. *Chem. Mater.* **2015**, *27*, 7149–7155. [CrossRef]
60. Zhou, Y.; Yang, M.; Kwun, J.; Game, O.S.; Zhao, Y.; Pang, S.; Padture, N.P.; Zhu, K. Intercalation crystallization of phase-pure α-HC(NH$_2$)$_2$PbI$_3$ upon microstructurally engineered PbI$_2$ thin films for planar perovskite solar cells. *Nanoscale* **2016**, *8*, 6265–6270. [CrossRef]
61. Adhikari, N.; Dubey, A.; Gaml, E.A.; Vaagensmith, B.; Reza, K.M.; Mabrouk, S.A.A.; Gu, S.; Zai, J.; Qian, X.; Qiao, Q. Crystallization of a perovskite film for higher performance solar cells by controlling water concentration in methyl ammonium iodide precursor solution. *Nanoscale* **2016**, *8*, 2693–2703. [CrossRef] [PubMed]
62. Futscher, M.H.; Lee, J.M.; McGovern, L.; Muscarella, L.A.; Wang, T.; Haider, M.I.; Fakharuddin, A.; Schmidt-Mende, L.; Ehrler, B. Quantification of ion migration in CH 3 NH 3 PbI 3 perovskite solar cells by transient capacitance measurements. *Mater. Horiz.* **2019**, *6*, 1497–1503. [CrossRef]
63. Bag, M.; Renna, L.A.; Adhikari, R.Y.; Karak, S.; Liu, F.; Lahti, P.M.; Russell, T.P.; Tuominen, M.T.; Venkataraman, D. Kinetics of ion transport in perovskite active layers and its implications for active layer stability. *J. Am. Chem. Soc.* **2015**, *137*, 13130–13137. [CrossRef] [PubMed]
64. Xiao, Z.; Yuan, Y.; Shao, Y.; Wang, Q.; Dong, Q.; Bi, C.; Sharma, P.; Gruverman, A.; Huang, J. Giant switchable photovoltaic effect in organometal trihalide perovskite devices. *Nat. Mater.* **2015**, *14*, 193–198. [CrossRef] [PubMed]
65. Yang, T.-Y.; Gregori, G.; Pellet, N.; Grätzel, M.; Maier, J. The significance of ion conduction in a hybrid organic–inorganic lead-iodide-based perovskite photosensitizer. *Angew. Chem. Int. Ed. Engl.* **2015**, *54*, 7905–7910. [CrossRef]
66. Azpiroz, J.M.; Mosconi, E.; Bisquert, J.; De Angelis, F. Defect migration in methylammonium lead iodide and its role in perovskite solar cell operation. *Energy Environ. Sci.* **2015**, *8*, 2118–2127. [CrossRef]
67. De Bastiani, M.; Dell'Erba, G.; Gandini, M.; D'Innocenzo, V.; Neutzner, S.; Kandada, A.R.S.; Grancini, G.; Binda, M.; Prato, M.; Ball, J.M.; et al. Ion migration and the role of preconditioning cycles in the stabilization of the J–V characteristics of inverted hybrid perovskite solar cells. *Adv. Energy Mater.* **2016**, *6*, 1501453. [CrossRef]
68. Li, C.; Tscheuschner, S.; Paulus, F.; Hopkinson, P.E.; Kießling, J.; Köhler, A.; Vaynzof, Y.; Huettner, S. Iodine migration and its effect on hysteresis in perovskite solar cells. *Adv. Mater.* **2016**, *28*, 2446–2454. [CrossRef]
69. Almora, O.; Guerrero, A.; Garcia-Belmonte, G. Ionic charging by local imbalance at interfaces in hybrid lead halide perovskites. *Appl. Phys. Lett.* **2016**, *108*, 043903.
70. Guerrero, A.; Garcia-Belmonte, G.; Mora-Sero, I.; Bisquert, J.; Kang, Y.S.; Jacobsson, T.J.; Correa-Baena, J.-P.; Hagfeldt, A. Properties of contact and bulk impedances in hybrid lead halide perovskite solar cells including inductive loop elements. *J. Phys. Chem. C* **2016**, *120*, 8023–8032.
71. Zarazua, I.; Bisquert, J.; Garcia-Belmonte, G. Light-induced space-charge accumulation zone as photovoltaic mechanism in perovskite solar cells. *J. Phys. Chem. Lett.* **2016**, *7*, 525–528. [CrossRef] [PubMed]

72. Kazuya, T. Comment on "Simulation of current–voltage curves for inverted planar structure perovskite solar cells using equivalent circuit model with inductance". *Appl. Phys. Express* **2017**, *10*, 059101.

73. Pockett, A.; Eperon, G.E.; Sakai, N.; Snaith, H.J.; Peter, L.M.; Cameron, P.J. Microseconds, milliseconds and seconds: Deconvoluting the dynamic behaviour of planar perovskite solar cells. *Phys. Chem.* **2017**, *19*, 5959–5970. [CrossRef] [PubMed]

74. Almora, O.; Cho, K.T.; Aghazada, S.; Zimmermann, I.; Matt, G.J.; Brabec, C.J.; Nazeeruddin, M.K.; Garcia-Belmonte, G. Discerning recombination mechanisms and ideality factors through impedance analysis of high-efficiency perovskite solar cells. *Nano Energy* **2018**, *48*, 63–72. [CrossRef]

75. Zarazua, I.; Han, G.; Boix, P.P.; Mhaisalkar, S.; Fabregat-Santiago, F.; Mora-Seró, I.; Bisquert, J.; Garcia-Belmonte, G. Surface Recombination and Collection Efficiency in Perovskite Solar Cells from Impedance Analysis. *J. Phys. Chem. Lett.* **2016**, *7*, 5105–5113. [CrossRef] [PubMed]